International Journal of Heat and Mass Transfer 217 (2023) 124700

Contents lists available at ScienceDirect

International Journal of Heat and Mass Transfer

journal homepage: www.elsevier.com/locate/ijhmt

Thermal conductivity of the cell wall of wood predicted by inverse analysis of 3D homogenization

Brahim Mazian *, El-Houssaine Quenjel, Patrick Perré

Université Paris-Saclay, CentraleSupélec, Laboratoire de Génie des Procédés et Matériaux, Centre Européen de Biotechnologie et de Bioéconomie (CEBB), 3 rue des Rouges Terres 51110 Pomacle, France

ARTICLE INFO

Keywords:
Anisotropy
CT scan
3D morphology
Poplar
Spruce

ABSTRACT

This work proposes an accurate prediction of the directional thermal conductivity of wood at the cell wall scale. To that purpose, the strategy combines the physical characterization at the macroscopic scale, the description of the cellular morphology, homogenization calculations and an inverse analysis. The first step consisted in measuring the macroscopic thermal conductivity using the Transient Plane Source (TPS) method in the three material directions of spruce and poplar. The values range from 0.10 to 0.31 $W m^{-1} K^{-1}$ depending on direction and species. The 3D morphology was acquired by micro-tomography and subsequently processed to generate a digital representation of the cellular structure. This representation is the input geometry in an homogenization procedure. Based on the results of this algorithm, the measurements of the solid fraction and the macroscopic values, we are able to determine the microscopic thermal conductivity of the cell wall λ_0^s, which is impossible to measure directly. λ_0^s was also found to be anisotropic with respective values of 0.6 and 1.0 $W m^{-1} K^{-1}$ in the transverse plane and the longitudinal direction.

1. Introduction

The building industry accounts for approximately 40% of final energy consumption and is responsible for more than 36% of greenhouse gas emissions in Europe, primarily due to heating, cooling, and air conditioning systems [1,2]. This is why the sector urgently needs strategies to reduce energy consumption and CO_2 emissions. One of them is to accelerate the use of new biobased materials or existing renewable materials as insulation products in building construction [3,4], as they accumulate several advantages: carbon sequestration, low content of transformation energy and good combination between structural and thermal behavior. Wood is among the most abundant renewable materials that need to be promoted as building materials.

Due to its biological origin, wood differs from other industrial materials, as it is not manufactured but produced by trees through secondary growth and subsequent lignification. This gives rise to a complex structure composed of vertically elongated cells, of which the secondary wall consists of an assembly of macro-molecules (cellulose, hemicelluloses, and lignins). In terms of mechanical behavior, the building brick of this secondary cell wall is a long, linear chain of cellulose arranged in crystalline bundles, called microfibrils, quasi-aligned along the longitudinal axis of the cell for the thick S2 layer. They structure the entire cell wall which is therefore anisotropic at the microscopic level [5,6]. The upper scale, the cellular organization, also shapes the macroscopic properties through its porous and anisotropic morphology [7,8]. This unique structure results in good thermal insulation properties (0.09 - 0.35 $W m^{-1} K^{-1}$) compared to other building materials such as aluminum (160 $W m^{-1} K^{-1}$), granite (2.8 $W m^{-1} K^{-1}$) and glass (1.4 $W m^{-1} K^{-1}$), together with excellent specific mechanical properties (stiffness and ultimate stress over density) [9–11].

The thermal conductivity of wood is then a crucial parameter, namely as input data for modeling tools, during processing or usage of wood [12–15]. However, the variability of wood properties, both within and between species, makes this task tedious. Usually, two primary conventional methods can be used to measure thermal conductivity: the steady-state or transient methods. The steady-state method consists in measuring the temperature difference across a sample dT/dx ($K m^{-1}$) with a known heat flow J ($W m^{-1}$), or vice versa, at steady-state. The steady-state method, such as the guarded hot plate [16] and the heat flow meter [17], can measure the thermal conductivity with

* Corresponding author.
E-mail addresses: brahim.mazian@centralesupelec.fr (B. Mazian), el-houssaine.quenjel@centralesupelec.fr (E.-H. Quenjel), patrick.perre@centralesupelec.fr (P. Perré).

https://doi.org/10.1016/j.ijheatmasstransfer.2023.124700
Received 28 June 2023; Received in revised form 31 August 2023; Accepted 8 September 2023
Available online 25 September 2023

high accuracy, but they require large samples and a long time to reach steady-state.

In the transient method, a heat flux is applied to the sample and the temperature response is recorded over time. This method is more versatile than the steady-state method as it can measure thermal properties in non-steady-state conditions and for small samples in a short measurement time. In this study, the hot-disk method, a type of transient method also known as the transient plane source (TPS) method, was considered for measuring the thermal properties of wood [18–20]. The hot-disk method was developed by Gustafsson to measure thermal properties and has the advantage of being able to measure both thermal conductivity and thermal diffusivity over a wide range of temperatures in a single measurement for isotropic materials. The relationship between thermal conductivity, thermal diffusivity, specific heat, and density can be expressed by an equation, making it possible to calculate all thermal properties in one measurement for isotropic materials with a known density. A theory has also been established for applying the hot-disk method to anisotropic materials, which requires separate measurements of specific heat and the density of the material. This method was successfully applied to many inorganic materials such as metal and glass [21,22], and it has been adopted in the ISO standard to measure the thermal properties of plastic materials [23].

As a way to address the tedious demand of experimental characterization, the actual performances of 3D imaging devices together with HPC (high-performance computing) allow the macroscopic properties to be predicted by upscaling from real 3D morphologies. This scaling prediction approach is an active field of research, whose basic theory comes from theoretical works on homogenization or volume averaging [24–27]. The first attempts to predict wood properties from its anatomical structure were simple models [28] or used computational solutions on simple virtual or real 2D cellular structures [29,30]. Nowadays, the cellular structure of wood can be easily obtained by micro- or nano-tomography using laboratory equipment [31–34] or using Synchrotron facilities [35,36,32,37]. For instance, the Finite Element method [38,39] and the Lattice Boltzmann method [40] have been employed to solve the homogenization equations and predict the directional thermal conductivities of 3D morphologies of wood. A finite volume scheme was proposed in [41] for the same purpose. An efficient algorithm was designed in [42] to reduce the computational cost by solving the stationary Fourier's model instead of the transient solution. However, one must keep in mind that up-scaling needs not only the morphology, but also the local properties (microscopic scale) to be supplied to predict the effective properties (macroscopic scale). In the case of wood, these local properties are very difficult to obtain because cell walls are not available as is. Direct measurements by scanning thermal microscopy (SThM) were tested [43]. However, the published work gives relative variations of the thermal conductivity in the cross-section of the cell wall rather than absolute values. In addition, this technique cannot give directional values of thermal conductivity. Indeed, the relative variations observed inside the secondary cell wall are mostly due to the change in orientation of the microfibril in the different layers. To overcome this experimental difficulty, a self-consistent scheme (a global up-scaling method) was proposed as a means to predict the cell wall properties from the assembly of the cell wall polymers (cellulose, hemicellulose and lignins) [44]. However, as the assessment of the directional conductivity of these polymers is itself based on strong assumptions, this virtual approach should be understood as an order of magnitude rather than as a method of determination.

This work proposes an original and accurate approach to determining the directional thermal conductivity of the wood cell wall. Upscaling is a way to change spatial scale: using the phase morphology of the heterogeneous phase and the local properties of these phases, the method is able to compute the effective (macroscopic) property as illustrated in Fig. 1.

Instead of this standard use where the measured value serves for validation purposes, an inverse analysis of a full homogenization strategy is proposed here. In fact, this idea was proposed several years ago [45], but considerable progress in imaging and computational methods has been required for its rigorous implementation in 3D. For example in [46,47], the authors consider the heat transfer model and utilize the TPS method for predicting the numerical thermal conductivity of composite materials (e.g. cementitious syntactic foams enriched with hollow glass microspheres). By applying a finite element solver, they were able to derive thermal conductivity values, demonstrating the effectiveness of their approach when investigating composite samples. In the present work, we adopt an inverse analysis strategy: the microscopic thermal conductivity values are identified to allow the macroscopic property, as computed by homogenization, to align with the macroscopic measurements.

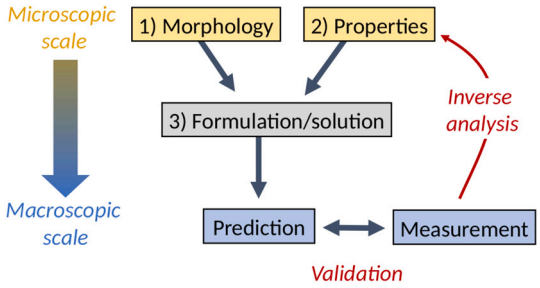

Fig. 1. The concept of inverse analysis applied to a complete up-scaling approach.

Using the aforementioned TPS method, measurements were performed to obtain the macroscopic thermal conductivity along the three orthotropic directions of wood. Two wood species were investigated: spruce and poplar. Besides, the same samples were scanned at high resolution using a nanotomograph. The 3D images were used to generate the real 3D morphology of the samples. A manual segmentation of the scanned sample was applied to frame the solid physical fraction of the sample, as measured by gravimetry. Then, the face interpolated scheme [48] was used to compute the discrete solution of Fourier's equation. Several computations were carried out to map the effect of density and local conductivity on the effective value. For each species and direction, the microscopic thermal conductivity was defined as the value that allows the predicted effective value equal to the measured value (arrow *Inverse analysis* in Fig. 1). For both species, the cell wall conductivity λ_0^s depicts an anisotropic ratio of the order of 2. As expected, the conductivity is larger along the crystalline direction of cellulose: the longitudinal conductivity is higher than the transverse values.

2. Materials and methods

2.1. Materials

Two wood species, poplar (*Populus euroamericana* Koster) and spruce (*Picea abies*) were investigated (Fig. 2). The poplar tree came from the forest in Auménancourtle-Petit and was supplied by the Huberlant sawmill in Cormicy. The spruce tree comes from a plantation in the Le Châtaignier forest in Riotord. The trees were collected with proper permission and cut into logs at the sawmill. The samples for the experiment were taken from a single, straight-grained, board without any defects. They were carefully cut along the longitudinal direction along which the natural variability of the wood is minimal. The sample size and preparation method were tailored to meet the requirements of the thermal conductivity test. The densities of spruce and poplar are 451 kg/m^3 and 348 kg/m^3, respectively.

2.2. Experimental setting

The thermal conductivity of the materials was measured using the C-therm Trident Thermal Conductivity Analyzer (from C-therm, Canada).

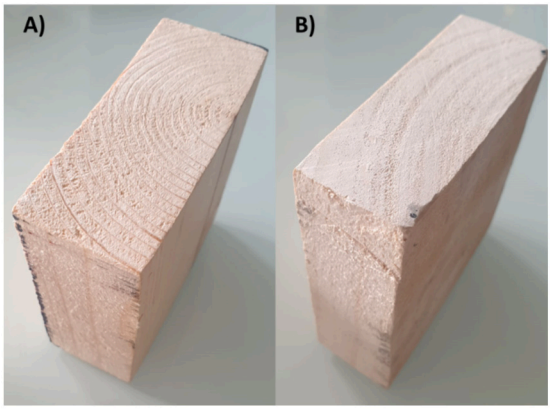

Fig. 2. Macroscopic images of the two wood species. A) Spruce, B) Poplar.

The Flex Transient Plane Source (TPS) technique, also known as the hot disk method or Gustafsson probe, was employed. This method imposes a constant heat flux on the sample and measures the temperature evolution. The flux is imposed via a user-defined input power P_0 (W) to the Hot Disk sensor, while its resistance evolution is calibrated to get its temperature. The Hot Disk sensor comprises a double nickel spiral covered by thin insulating sheets and is placed between two identical samples being tested, see Fig. 3.

During measurement, the sensor behavior can be described as a time-dependent resistance $R(t)$:

$$\left[\begin{array}{l} R(t) = R_0\left(1 + a\ \Delta T(\tau)\right) \\ \tau = \left(\frac{t}{\theta}\right)^{\frac{1}{2}}, \quad \theta = \frac{r^2}{\alpha} \end{array}\right] \tag{2.1}$$

Where R_0 is the initial resistance of a Hot Disk sensor, a is the temperature coefficient of resistance (TCR), $\Delta T(\tau)$ is the time-dependent temperature changing of the Hot Disk sensor. θ stands for characteristic time, r (mm) is the outer radius of the sensor and α is the thermal diffusivity of the tested material.

The temperature increase of the specimen surface can be determined by solving the heat conduction equation for a semi-infinite medium, as demonstrated in [18,49,23]. Accordingly, the average temperature rise of the double spiral heater can be expressed as follows:

$$\Delta T(\tau) = P_0\left(\pi^{3/2} r \lambda\right)^{-1} D(\tau), \tag{2.2}$$

where P_0 is the power dissipation from the heater, λ is the thermal conductivity of the material sample and $D(\tau)$ is a dimensionless time function [18,49,23].

The temperature increase of the sensor during the transient period should be linearly proportional to a function $D(\tau)$. Therefore, it can be possible to fit ΔT as a function of $D(\tau)$ with a straight line as long as the relationship between t and τ is known. The slope of the obtained line is $P_0\left(\pi^{3/2} r \lambda\right)^{-1}$, which is used to extract thermal conductivity.

Equation (2.2) is applied when the tested material is isotropic. However, if the specimen is anisotropic and has different thermal properties along the $x-$ and y-axes compared to the z-axis, the temperature increase of a Hot Disk sensor surrounded by this material over time is described as follows:

$$\Delta T(\tau(\alpha_x)) = P_0\left(\pi^{3/2} r (\lambda_x \lambda_z)^{1/2}\right)^{-1} D(\tau(\alpha_x)), \tag{2.3}$$

where λ_x and λ_z are the thermal conductivities along the x-axis (radial) and z-axis (axial), respectively.

The radial thermal diffusivity α_x in the plane of the probe (disk) is fitted to allow the temperature evolution $\Delta T(\tau(\alpha_x))$ to vary linearly with function $D(\tau(\alpha_x))$. Once done, provided that both the density (ρ) and specific heat capacity (C_p) of the material are known (measured by independent methods), the thermal conductivities in the x-axis (λ_x) and z-axis (λ_z) can be established through a single hot-disk measurement. To obtain λ_x, the fitted diffusivity value is used to calculate λ_x using the classical relation:

$$\lambda_x = \alpha_x \rho C_p. \tag{2.4}$$

The axial thermal conductivity (λ_z) can subsequently be determined via the experimental slope $m = \Delta T(\tau(\alpha_x))/D(\tau(\alpha_x))$ of Equation (2.3):

$$\lambda_z = \left(\frac{P_0}{\pi^{3/2} \cdot r \cdot m}\right)^2 \frac{1}{\lambda_x}. \tag{2.5}$$

As the thermal conductivities of wood are not equal in the plane of the sensor, the value of λ_x is an average of the that directions and was never used as a measurement. It was just used to determine the axial conductivity. The hot-disk measurements were then conducted successively for the three material directions of wood: radial, tangential, and longitudinal. The samples were prepared in such a way that, for each measurement, one of the main wood directions (radial, tangential or longitudinal) was aligned with the axial direction (λ_z), as depicted in Fig. 4. As a result, the thermal conductivity obtained in the axial direction (depth) is, successively, the radial, tangential, and longitudinal thermal conductivity. Hot Disk Kapton sensors with radii of 13 mm were used. The input power and duration of the measurements were selected to achieve the necessary probing depth and characteristic time. To maintain constant pressure on the sensor, the sensor was placed between two plates inside the sample holder as shown in Fig. 3. The measurements were repeated several times, with three to five repetitions per set of parameters. The experiments were conducted under

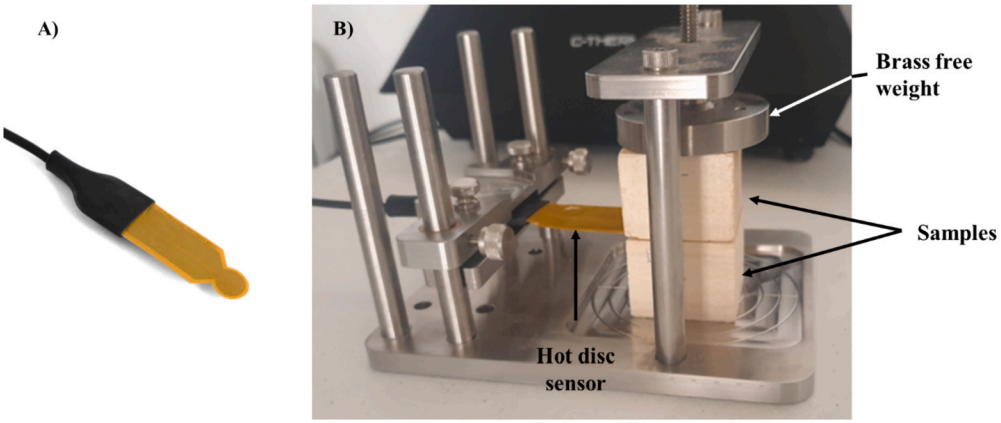

Fig. 3. The C-therm Trident Thermal Conductivity Analyzer A) hot disk sensor B) hot sensor setup depicting hot disk sensor sandwiched between twin wood samples.

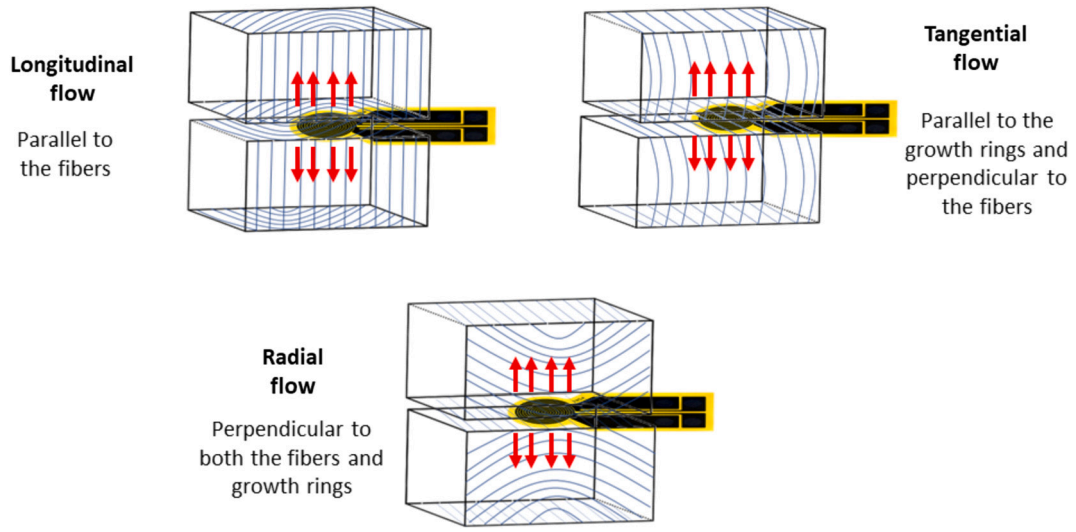

Fig. 4. Schematic representation of the symmetrical configurations obtained with twin samples to measure the thermal conductivity along the three material directions (radial, tangential, and longitudinal).

Table 1
Specific heat values of oven-dry spruce and poplar measured using C80 technique (values at 25 °C).

Specific heat ($J\,Kg^{-1}\,K^{-1}$)	Spruce	Poplar
Value	1376 ± 51	1302 ± 11

ambient conditions and at room temperature. The time intervals between measurements were long enough to allow the temperature field to equilibrate.

2.3. Specific heat measurement

The heat capacity measurement was carried out using a C80 Calvet calorimeter from Setaram, employing a high-pressure air-tight cell with an 8.5 cm^3 volume. Sample masses ranging from $1g$ to $2g$ were used. In the case of hygroscopic products, preliminary results pointed out that the perturbation due to water evaporation during heating up is not negligible, even with a sealed crucible. Indeed, one part of bound water evaporates into the gaseous volume of the crucible and the corresponding latent heat of evaporation is included as a contribution to the heat capacity. Accordingly, the samples were dried in an oven at 378 K overnight before the measurement. The sample was placed in the measurement cell, while the reference cell remained empty. The heating protocol was as follows. After stabilizing the heat flow signal for 90 minutes, the system was maintained at a constant temperature of 313 K for another 90 minutes. Subsequently, the temperature was raised to 383 K at a rate of 0.2 K/min, followed by an isothermal step of 90 minutes at 383 K. Throughout the heating process, variations in heat flow were recorded by the Setsoft 2000 software. Values obtained for the two wood species are shown in Table 1.
It should be noted that the obtained specific heat capacity values correspond to the oven-dry state (Cp_{dry}). These values were corrected to obtain the heat capacity at the actual moisture content during TPS measurements, Cp_X, assuming additivity of heat capacities and assuming bound water to have the same heat capacity as liquid water:

$$\rho_X Cp_X = \frac{\rho_X Cp_{dry}}{1+X} + \frac{\rho_X X Cp_{water}}{1+X} \tag{2.6}$$

Where ρ_X is the sample density measured during TPS measurement (moist mass over moist volume) and X is the moisture content obtained by oven-dry mass determination after the test.

2.4. Tomography and segmentation

We used tomography to capture the structural morphology of the wood samples. Cylindrical samples, with millimeter-size diameters, were prepared to obtain high-resolution scans using a lab X-ray nanotomograph (UltraTom by RX-solutions). The nano-focus source with a tungsten filament and the CCD imager was mounted on the device to obtain a resolution of the order of 1 μm for a scanning time of at least four hours. Fig. 5 depicts the full scan of the spruce and poplar samples.

The high-resolution 3D scans, as obtained from tomography after image reconstruction, require further processing before being used as morphology input in the computational simulation code. At first, the image files are extremely large, which imposes an adequate ROI (Region of Interest) to be chosen within the sample. This sub-volume is a parallelepiped whose center and dimensions must be selected. At this stage, it is possible to apply the automatic thresholding technique of Otsu to produce the binary image. The goal is to separate and identify the present two phases (gas and solid) and generate the morphology's hexahedral mesh. Manual thresholding was also performed to obtain solid fractions capable of framing the physical fraction. The image processing procedure was implemented in Python using the *scikit-image* package.

2.5. Up-scaling procedure

Following Fig. 1, the up-scaling methods such as homogenization [25,27] is a technique that allows the prediction of the macroscopic property of materials, in our case the effective thermal conductivity, by solving a specific problem. The first step is to use the local properties of the present phases within the medium and the morphological structure of the phases. In the present work, the structure is described by image-based meshing of the real phase morphology gained by high-resolution CT scans. The local, microscopic, conductivity of the cell wall cannot be measured physically at the pore scale, but the macroscopic property is accessible through measurements. Taking into account these macroscopic values, it is possible to tune the microscopic thermal conductivity to get the correct macroscopic value by homogenization.

In the present work, the method was applied to real 3D morphologies of wood. Before going further, let us briefly sketch the numerical resolution of Fourier's problem within the domain occupied by the sample. Let $\Omega = (x_0, x_m) \times (y_0, y_n) \times (z_0, z_p)$ account for the segmented morphology. Consider the stationary heterogeneous heat equation written as

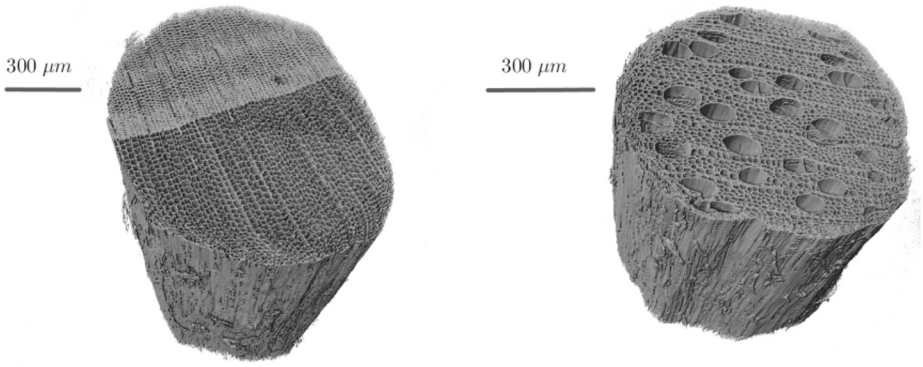

Fig. 5. Scanned sample of spruce (left) and poplar (right).

$$\begin{cases} -\nabla\cdot\left(\lambda^0(\mathrm{x})\nabla u\right) &= 0, \quad \text{in} \quad \Omega, \\ u &= u_D, \quad \text{on} \quad \partial\Omega^{Dir}, \\ \lambda^0(\mathrm{x})\nabla u\cdot\vec{\mathbf{n}} &= 0, \quad \text{on} \quad \partial\Omega^{N}, \end{cases} \tag{2.7}$$

where $\partial\Omega = \partial\Omega^{Dir}\cup\partial\Omega^{N}$ and λ^0 is the microscopic thermal conductivity. In the case of a morphology defined by a real structure, the classical, proper, periodic conditions fail as the cell wall could be connected, on the opposite face, to gas or vice-versa. The best way to pave the space by the computed REV in this case is to consider that all planes of the REV are indeed planes of symmetry. This turns in Dirichlet conditions on the opposite faces orthogonal to the imposed macroscopic gradient and Newmann conditions (fluxes equal to zero) on the four remaining faces parallel to the macroscopic gradient. Therefore, for the computation of the conductivity in, let's say, the x direction, one sets $u_D = 1$ on the face $\{x = x_0\}$ and $u_D = 0$ on the opposite face $\{x = x_m\}$. Adiabatic Neumann boundary conditions are imposed on the rest of the boundary $\partial\Omega^N$.

In order to get the computational solution of (2.7), we apply the 3D face interpolated scheme to Fourier's law [50]. This methodology can deal with general hexahedral meshes. Not only it offer a cheap computational cost, but it also provides accurate results, see [48] for more details. First, the domain Ω is discretized using the hexahedral mesh $\mathcal{T}$ generated from the sample's morphology. The volumes of this partition are denoted by V. Then, in each volume, the approximate gradient $\nabla_V u_h$ is reconstructed using three directions offered by the opposite faces of the cell. As a consequence, the numerical temperature is derived by solving the linear system obtained from the discrete variational formulation

$$\int_\Omega \lambda_h^0(\mathrm{x})\nabla u_h(\mathrm{x})\cdot\nabla\varphi_h(\mathrm{x})\,\mathrm{dx} = \sum_{V\in\mathcal{T}} |V|\,\lambda_V^0\nabla_V u_h\cdot\nabla_V\varphi_h = 0, \tag{2.8}$$

where φ_h is a piecewise constant function on the mesh vertices. The equation associated to the node $i\in\Omega\setminus\Omega^{Dir}$ is obtained by taking $\varphi_i = 1$ and $\varphi_j = 0$ for all $(j\neq i)$ in Eq. (2.8).

Finally, one can deduce the predicted thermal conductivity by assessing the ratio of the boundary flux $\langle \mathrm{q}_x^{\partial\Omega^{Dir}}\rangle$ to the global gradient $\delta u/\left|x_m - x_0\right|$. More importantly, using the Dirichlet and Neumann boundary conditions separately, one has

$$\lambda_R = \frac{\langle \mathrm{q}_x^{\partial\Omega^{Dir}}\rangle\times\left|x_m - x_0\right|}{\delta u}, \quad \lambda_\tau = \frac{\langle \mathrm{q}_y^{\partial\Omega^{Dir}}\rangle\times\left|y_n - y_0\right|}{\delta u},$$
$$\lambda_L = \frac{\langle \mathrm{q}_z^{\partial\Omega^{Dir}}\rangle\times\left|z_p - z_0\right|}{\delta u}.$$

3. Results and discussion

3.1. Experimental values

The measured thermal conductivity values of studied wood ranged from 0.10 to 0.31 $\mathrm{W\,m^{-1}\,K^{-1}}$ (Fig. 6 and detailed in Table 2). For both species, the thermal conductivity in the longitudinal direction (L) was found to be significantly higher than in the radial (R) and tangential (T) directions. For instance, the thermal conductivity of spruce wood in the L direction was 0.311 W/m K, while in the R and T directions, it was 0.118 W/m K and 0.122 W/m K, respectively. Poplar wood demonstrated similar results, with a thermal conductivity of 0.235 W/m K in the L direction and 0.108 W/m K and 0.105 W/m K in the R and T directions, respectively. In L direction, the heat conductivity of the solid phase is high because the heat flow is parallel to the cellulose microfibrils. In addition, in this direction, the phases of the porous medium are organized in parallel as the flow is along the axial direction of cells. Altogether, it is well known that, in wood, the longitudinal conductivity is higher than in the R and T directions [50].

Furthermore, it can be discerned from the same figure that spruce has a slightly higher thermal conductivity than poplar, which can be attributed to their difference in density. As the solid phase is the most conductive for thermal transfer, a higher density increases the thermal conductivity. In addition to the density, the difference between the two species is believed to be due to the difference in cellular structure

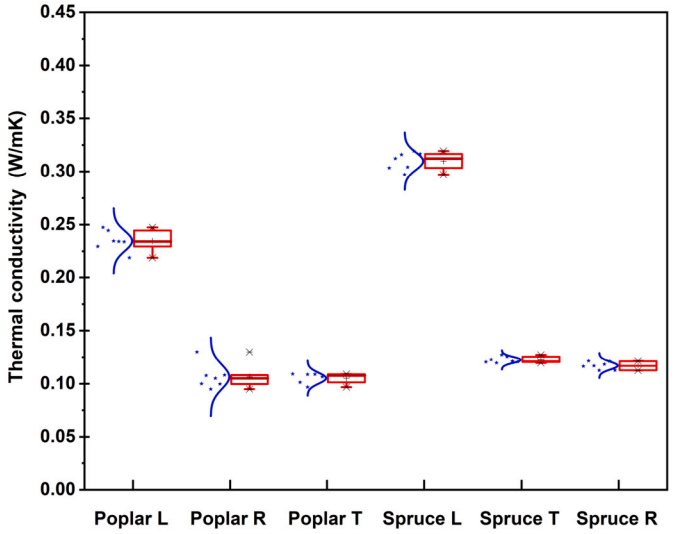

Fig. 6. Directional thermal conductivity values of spruce and poplar samples measured using the TPS method.

Table 2
Mean values obtained for the spruce and poplar sample.

Sample	λ_R	λ_τ	λ_L
Spruce ($\mathrm{W\,m^{-1}\,K^{-1}}$)	0.118 ± 0.004	0.122 ± 0.003	0.311 ± 0.008
Poplar ($\mathrm{W\,m^{-1}\,K^{-1}}$)	0.108 ± 0.011	0.105 ± 0.005	0.235 ± 0.010

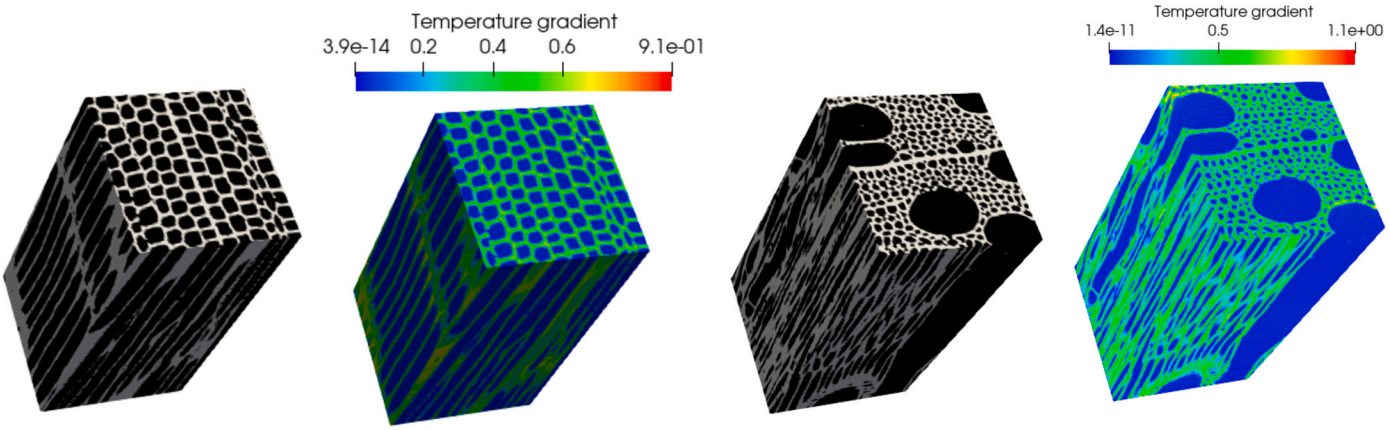

Fig. 7. From left to right: binary morphology, temperature gradient for spruce and poplar respectively. (For interpretation of the colors in the figure(s), the reader is referred to the web version of this article.)

Table 3
Solid fraction of spruce and poplar as a function of the REV size.

Sample	REV1	REV2	REV3	REV4	REV5	REV6
Size	32×32×63	64×64×127	96×96×191	128×128×255	160×160×319	192×192×383
Spruce	0.309	0.324	0.316	0.318	0.3160	0.323
Poplar	0.337	0.328	0.274	0.250	0.2389	0.259

between spruce, a softwood mainly made of tracheids and poplar, a pore-diffuse hardwood, which presents a dual-scale organization (vessels and cells). These results are consistent with previous studies in the literature [51,52].

The anisotropy ratio in the cross-section (R-T plane) is indeed a frequently debated topic, and the outcomes can vary based on the wood type. Maeda et al. (2021) [52] observed comparable values in the R and T directions, particularly for woods with a density below 500 kg/m^3. Our study focused on woods with densities under 500 kg/m^3, which aligns with Maeda's observations. Steinhagen (1977) [53] explains that the conductivity ratio between these two orientations (tangential and radial) is influenced by various structural elements of the anatomical pattern. For example, oak, which has a large number of ray cells, showed a significant difference between tangential and radial conductivities, while spruce, which has fewer ray cells, exhibited a smaller or no difference in the conductivity. It is interesting to mention that our work is able to distinguish these two effects of the macroscopic conductivity: i) the phase organization, which is considered by the homogenization with image-based meshing of the real anatomy and ii) the anisotropy of the cell wall itself which is an input parameter of the up-scaling calculation but that will be determined by inverse analysis.

3.2. Convergence test

In this first numerical experiment, a convergence test was conducted with the guess value ($0.5\ \mathrm{W\,m^{-1}\,K^{-1}}$) of the microscopic thermal conductivity. The objective is to find a Representative Elementary Volume (REV) whose size is sufficient for stabilizing the effective property. First, the anatomical axis of the wood sample was aligned with the standard Cartesian directions. The sequence of the considered REVs is taken within the full 3D image of the sample. They are denoted by $\mathrm{REV}_i = (x_0, x_m^i) \times (y_0, y_m^i) \times (z_0, z_p^i)$ where

$$x_m^i = x_0 + 32 \times i, \quad y_n^i = y_0 + 32 \times i, \quad z_p^i = (64 \times i) - 1, \quad \text{for } i = 1, \cdots, 6.$$

In the case of spruce, we set $(x_0, y_0, z_0) = (1155, 870, 555)$ as the center. For poplar, we consider the center $(x_0, y_0, z_0) = (940, 940, 555)$. Running the Python script of the segmentation yields the binary morphology of spruce and poplar exhibited in Fig. 7.

Table 4
The thermal conductivity of spruce and poplar in the orthotropic directions as a function of the REV size.

Sample	λ ($\mathrm{W\,m^{-1}\,K^{-1}}$)	REV1	REV2	REV3	REV4	REV5	REV6
Spruce	λ_R	0.112	0.115	0.114	0.116	0.114	0.118
	λ_τ	0.117	0.123	0.119	0.117	0.115	0.116
	λ_L	0.167	0.172	0.1707	0.170	0.169	0.171
Poplar	λ_R	0.145	0.125	0.110	0.101	0.095	0.104
	λ_τ	0.085	0.104	0.083	0.074	0.075	0.080
	λ_L	0.181	0.174	0.150	0.140	0.135	0.142

Based on literature [41,42,50], let us set local thermal conductivity λ^0 for the two phases such that $\lambda_0^s = 0.5\ \mathrm{W\,m^{-1}\,K^{-1}}$, for solid and $\lambda_0^g = 0.023\ \mathrm{W\,m^{-1}\,K^{-1}}$ for gas. The numerical solution of the discretized model (2.7) is exhibited in Fig. 7 for spruce and poplar. In this case, Dirichlet boundary conditions are imposed on the lower and the upper faces of the z-direction. The gradient distribution highlights that the cell walls are the conducting phase.

The computed solid fractions are presented in Table 3. The convergence is noticed in the last volumes as the size becomes important. The corresponding predicted thermal conductivities are given in Table 4. For both species, the longitudinal conductivities are larger than the transverse ones. As the cell wall conductivity was assumed isotropic for these preliminary tests, this macroscopic anisotropy is solely due to the phase morphology distribution. The transverse values of spruce are quasi-similar, which indicates that the macroscopic value is at the same distance between the pure series and pure parallel models, whatever the transverse direction. However, a significant difference is observed for poplar, which is consistent with the elongated shape of vessels in the radial direction.

In all cases, the computed values converge, whatever the direction, as the REV size increases. This successful convergence test allows us to move on to the inverse analysis. Table 4 shows that the computed thermal conductivity converges from the fourth size. Therefore, a REV with the size $160 \times 160 \times 319$ voxels will be used in the following.

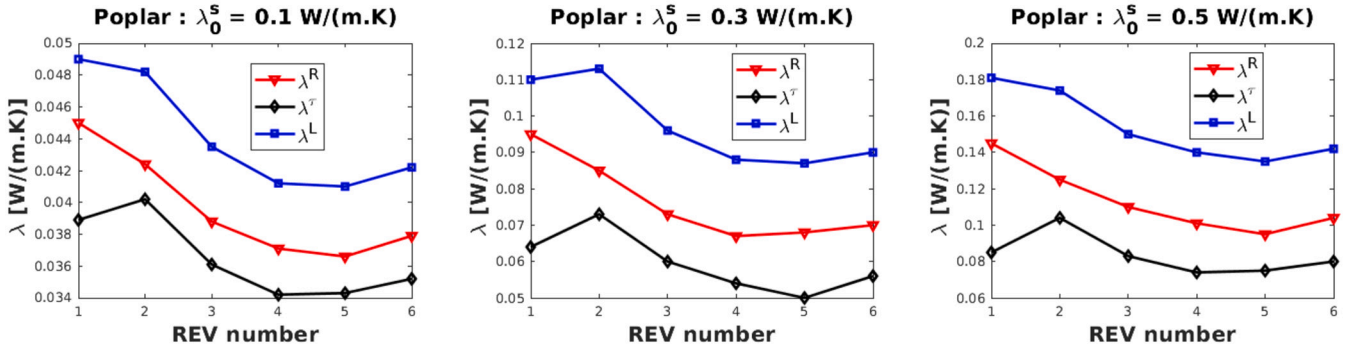

Fig. 8. Convergence of the macroscopic thermal conductivity in the case of poplar for different values of $\lambda_0^s \in \{0.1, 0.3, 0.5\}$ [W.m^{-1}.K^{-1}].

Fig. 8 exhibits the convergence of the macroscopic thermal conductivity *versus* the REV size for the poplar sample. Three values of the local property are considered $\lambda_0^s \in \{0.1, 0.3, 0.5\}$ [W m^{-1} K^{-1}]. It is shown that the choice of λ_0^s does not greatly impact convergence behavior. Indeed, the property is unstable on the first volumes. As it stabilizes afterward, the last volumes can be considered Representative. This might be quite questionable for poplar which presents a dual-scale porosity (vessels and cell lumens). However, we were limited by the CPU time as the inverse procedure proposed in this study requires many runs to be performed. The REV size used here can be considered fairly good for spruce and acceptable for poplar when looking at Fig. 8.

3.3. Inverse analysis

This section is devoted to the determination of the local values of conductivity (cell wall scale) by inverse analysis of the 3D homogenization procedure. This was completed to determine the microscopic thermal conductivity, λ_0^s, for the two species and the three material directions. For this purpose, the known, isotropic, conductivity of the air λ_0^g was fixed while the cell wall conductivity was mapped by discrete values over a range of values:

$$\lambda_i^s = (0.4 + i \times 0.02)\ \mathrm{W\,m^{-1}\,K^{-1}},\ \text{for all}\ , i = 0, \cdots, 40. \tag{3.1}$$

As explained in Section 2.4, manual thresholding was applied to ensure that the resulting solid fractions encompass the actual solid fraction, determined from density. The solid fraction is simply computed by assuming the intrinsic cell wall density to be close to 1500 kg m^{-3} [50]. The physical solid fraction ε_s^P is then $457/1500 = 0.305$ for spruce and $348/1500 = 0.232$ for poplar. The manual thresholding was performed to get a lower bound ε_s^ℓ smaller than ε_s^P as well as an upper one ε_s^u larger than ε_s^P.

The homogenization values were then computed for all discrete values of microscopic cell wall conductivity and the two bounds of solid fraction ($\lambda^{i,\ell}$, $\lambda^{i,u}$ for each discrete value of local conductivity). From this full mapping, we selected the two values of i, i_0 and i_1 such that the physical λ of the sample is bounded as follows

$$\lambda^{i_0,\ell} \le \lambda \le \lambda^{i_1,u}.$$

From this set of runs, we obtained a data set giving, for each direction, the macroscopic conductivity as a function of the microscopic cell wall conductivity, for the various solid fractions obtained by the different thresholding values. Finally, a bilinear interpolation over the solid fraction and the macroscopic conductivity allows to infer the adequate microscopic conductivity λ_0^s able to give, by homogenization, the measured macroscopic conductivity λ. Fig. 9 shows the results of the extrapolation strategy, i.e., the microscopic thermal conductivity in terms of the solid fraction and the macroscopic thermal conductivity for spruce and poplar species for each orthotropic direction. One can see the combined effects of microscopic conductivity (color scale) and the solid fraction (x-axis) on the macroscopic conductivity (y-axis). The intercept of the correct solid fraction (arrow 1 in Fig. 9) and measured conductivity (arrow 2 in Fig. 9) is designed by a marker in each subplot. The identified microscopic value λ_0^s can be seen on the color scale (arrow 3 in Fig. 9).

Table 5
Microscopic λ_0^s associated to the results of predictions and measurements.

Sample	ε_s^M	λ (W/(m K))	λ_0^s (W/(m K))	Macroscopic value
Spruce	0.304	λ_R	0.556	0.118
		λ_τ	0.600	0.122
		λ_L	1.003	0.311
Poplar	0.232	λ_R	0.582	0.108
		λ_τ	0.899	0,104
		λ_L	0.950	0.235

Table 5 reports the identified values of the microscopic thermal conductivity of the considered samples along the radial, tangential and longitudinal directions: this table summarizes the key results of this work. Similarly to the macroscopic level, it is observed that the ratio of anisotropy between the transverse plane and the L-direction is around two at the pore scale for spruce. This is consistent with the macro-molecular structure of the cell wall, with cellulose chains aligned along the cell axis [50]. A similar conductivity was found for poplar in the longitudinal direction (0.950 W/(m K) instead of 1.003 W/(m K) for spruce). Poplar is however different in the transverse plane. As already commented, the homogenized conductivity is larger in the radial direction than in the tangential direction, which is consistent with the elongated shape of vessels. However, the measured values are almost isotropic in the plane. Consequently, the identified conductivity of the cell wall is larger in the tangential direction ($\lambda_R = 0.582$ W/(m K) and $\lambda_\tau = 0.899$ W/(m K)). This could be explained by the difference in thermal behavior between the cell wall of fibers and vessels, or by an overestimation of the density of ray cells by the thresholding. One might also note that the convergence is less obvious for poplar, due to the double porosity distribution (Table 4). The boundary conditions applied to the unit cell assume this unit cell to be symmetrical. For vessels touching the border, this is likely to create, by symmetry, large tangential inclusions of low conductivity. Further works are in progress in our team to parallelize the code, which is required to work on larger unit cells while keeping the required spatial resolution required to represent correctly the cell wall geometry. In conclusion, the results obtained for spruce in the transverse plane seem more reliable than those for poplar. For the intrinsic properties of the secondary wall, we therefore propose to use the values 0.6 and 1.0 W m^{-1} K^{-1}, respectively in the transverse plane and in the longitudinal direction.

4. Conclusion

This work is devoted to the determination of the direction of thermal conductivities of the wood cell wall. As this value is very difficult, if not

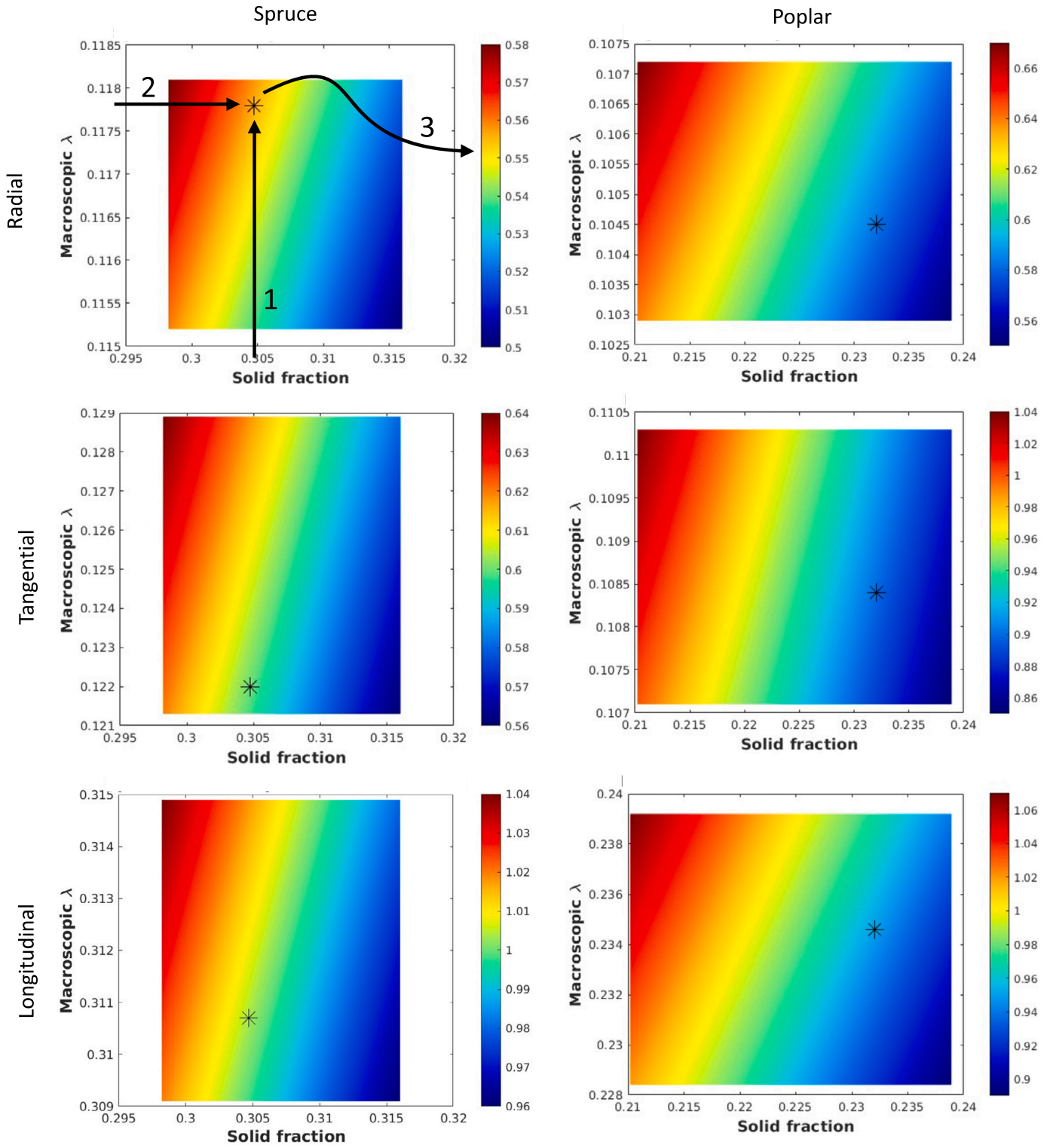

Fig. 9. Prediction of the macroscopic conductivity by homogenization (y-axis) for various values of solid fraction (x-axis) as a function of the microscopic value (color scale). Using the measured values of solid fraction(1) and macroscopic conductivity (2) to predict the suitable microscopic thermal conductivity (3). Results of spruce (left) and poplar (right) in the radial, tangential and longitudinal directions.

impossible, to measure directly, a novel approach, based on the inverse analysis of a full 3D homogenization is proposed.

The method includes the experimental characterization at the macroscopic level, high-resolution tomographic scans of the wood samples, the generation of a mesh from the real morphology and the computational solution of the homogenization problem. The solution of the heterogeneous Fourier's equation was obtained by the robust and accurate 3D face interpolated scheme. The work was conducted for two wood species: spruce and poplar.

Homogenization was used here as an inverse procedure: for each species and each material direction (Radial, Tangential and Longitudinal), the macroscopic value was computed for discrete values of local

conductivity and solid fraction. The local value was then defined as the value able to predict the measured conductivity for the right solid fraction. The cell wall conductivity was found to be highly anisotropic, with a factor of the order of 2. The cell wall is more conductive in the longitudinal direction (1.003 $W\,m^{-1}\,K^{-1}$ and 0.950 $W\,m^{-1}\,K^{-1}$ respectively for spruce and poplar).

CRediT authorship contribution statement

Brahim Mazian: Conceptualization; Methodology; Validation; Formal analysis; Investigation; Data Curation Management; Writing – Original Draft; Visualization. **El-Houssaine Quenjel:** Conceptualization; Methodology; Validation; Formal analysis; Investigation; Data Curation Management; Writing – Original Draft; Visualization. **Patrick Perré:** Conceptualization; Methodology; Formal analysis; Investigation; Resources; Data Curation Management; Writing – Review and Editing; Supervision; Project administration; Funding acquisition.

Declaration of competing interest

The authors declare that they have no known competing financial interests or personal relationships that could have appeared to influence the work reported in this paper.

Data availability

Data will be made available on request.

Acknowledgements

Communauté urbaine du Grand Reims, Département de la Marne, Région Grand Est and European Union (FEDER Champagne-Ardenne 2014-2020) are acknowledged for their financial support to the Chair of Biotechnology of CentraleSupélec and the Centre Européen de Biotechnologie et de Bioéconomie (CEBB).

References

[1] A.S. Ahmad, M.Y. Hassan, M.P. Abdullah, H.A. Rahman, F. Hussin, H. Abdullah, R. Saidur, A review on applications of ann and svm for building electrical energy consumption forecasting, Renew. Sustain. Energy Rev. 33 (2014) 102–109.
[2] K. Amasyali, N.M. El-Gohary, A review of data-driven building energy consumption prediction studies, Renew. Sustain. Energy Rev. 81 (2018) 1192–1205.
[3] A. Galimshina, M. Moustapha, A. Hollberg, P. Padey, S. Lasvaux, B. Sudret, G. Habert, Bio-based materials as a robust solution for building renovation: a case study, Appl. Energy 316 (2022) 119102.
[4] B. Mazian, E. Wirquin, K. Aguibi, P. Martin, L. Chaveriat, V. Dubois, Effect of mixing conditions on the density, morphology, thermal and mechanical properties of mineral foam, J. Build. Eng. 52 (2022) 104410.
[5] R. Mark, Cell Wall Mechanics of Tracheids, 1967.
[6] R.M. Rowell, R. Pettersen, J.S. Han, J.S. Rowell, M.A. Tshabalala, Cell wall chemistry, in: Handbook of Wood Chemistry and Wood Composites, vol. 2, 2005, pp. 33–72.
[7] F. Kollmann, W. Côté, Principles of Wood Science and Technology: I Solid Wood, Springer, 1968.
[8] H.H. Bosshard, Holzkunde: Band 2 Zur Biologie, Physik und Chemie des Holzes, Birkhäuser Verlag, Basel, 1984.
[9] Database of constructive solutions, http://cte-web.iccl.es/materiales.php.
[10] L. Gustavsson, A. Joelsson, Life cycle primary energy analysis of residential buildings, Energy Build. 42 (2) (2010) 210–220.
[11] W. Sonderegger, S. Hering, P. Niemz, Thermal Behaviour of Norway Spruce and European Beech in and Between the Principal Anatomical Directions, 2011.
[12] W. Olek, J. Weres, R. Guzenda, Effects of Thermal Conductivity Data on Accuracy of Modeling Heat Transfer in Wood, 2003.
[13] P. Perré, Fundamentals of Wood Drying, AR BO. LOR Nancy, 2007.
[14] J. Delgado, N.M. Ramos, E. Barreira, V.P. De Freitas, A critical review of hygrothermal models used in porous building materials, J. Porous Media 13 (3) (2010).
[15] P. Perré, R. Rémond, G. Almeida, P. Augusto, I. Turner, State-of-the-art in the mechanistic modeling of the drying of solids: a review of 40 years of progress and perspectives, Dry. Technol. 41 (6) (2023) 817–842.
[16] ISO 8302 Standard, Thermal Insulation—Determination of Steady-State Thermal Resistance and Related Properties—Guarded Hot Plate Apparatus. International Organization for Standardization, 1991.
[17] ISO 8301 Standard, Thermal Insulation—Determination of Steady-State Thermal Resistance and Related Properties—Guarded Hot Plate Apparatus. International Organization for Standardization, 1991.
[18] S.E. Gustafsson, Transient plane source techniques for thermal conductivity and thermal diffusivity measurements of solid materials, Rev. Sci. Instrum. 62 (3) (1991) 797–804.
[19] B.M. Suleiman, J. Larfeldt, B. Leckner, M. Gustavsson, Thermal conductivity and diffusivity of wood, Wood Sci. Technol. 33 (1999) 465–473.
[20] S. Lagüela, P. Bison, F. Peron, P. Romagnoni, Thermal conductivity measurements on wood materials with transient plane source technique, Thermochim. Acta 600 (2015) 45–51.
[21] A.A. Trofimov, J. Atchley, S.S. Shrestha, A.O. Desjarlais, H. Wang, Evaluation of measuring thermal conductivity of isotropic and anisotropic thermally insulating materials by transient plane source (hot disk) technique, J. Porous Mater. 27 (2020) 1791–1800.
[22] D. Vitiello, B. Nait-Ali, N. Tessier-Doyen, T. Tonnesen, L. Laím, L. Rebouillat, D.S. Smith, Thermal conductivity of insulating refractory materials: comparison of steady-state and transient measurement methods, Open Ceram. 6 (2021) 100118.
[23] ISO 22007-2 Standard, Plastics—Determination of Thermal Conductivity and Thermal Diffusivity—Part 2: Transient Plane Heat Source (Hot Disc) Method. International Organization for Standardization, 2015.
[24] P.M. Suquet, Homogenization Techniques for Composite Media, Lecture Notes in Physics, vol. 272, Springer-Verlag, 1985.
[25] E. Sanchez-Palencia, A. Zaoui, Homogenization Techniques for Composite Media, vol. 272, 1987.
[26] M. Quintard, S. Whitaker, Transport in ordered and disordered porous media ii: generalized volume averaging, Transp. Porous Media 14 (1994) 179–206.
[27] U. Hornung, Homogenization and Porous Media, vol. 6, Springer Science & Business Media, 1996.
[28] J.F. Siau, A geometrical model for thermal conductivity, Wood Fiber Sci. (1970) 302–307.
[29] P. Perré, I. Turner, Determination of the Material Property Variations Across the Growth Ring of Softwood for Use in a Heterogeneous Drying Model. Part 2. Use of Homogenisation to Predict Bound Liquid Diffusivity and Thermal Conductivity, 2001.
[30] P. Perré, G. Almeida, M. Ayouz, X. Frank, New modelling approaches to predict wood properties from its cellular structure: image-based representation and meshless methods, Ann. For. Sci. 73 (2016) 147–162.
[31] J. Van den Bulcke, M. Boone, J. Van Acker, M. Stevens, L. Van Hoorebeke, X-ray tomography as a tool for detailed anatomical analysis, Ann. For. Sci. 66 (5) (2009) 1–12.
[32] C.R. Brodersen, Visualizing wood anatomy in three dimensions with high-resolution x-ray micro-tomography (μct)–a review, in: Wood Structure in Plant Biology and Ecology, 2013, pp. 80–96.
[33] J.P. Lancha, P. Perré, J. Colin, P. Lv, N. Ruscassier, G. Almeida, Multiscale investigation on the chemical and anatomical changes of lignocellulosic biomass for different severities of hydrothermal treatment, Sci. Rep. 11 (1) (2021) 1–16.
[34] P. Perré, D.M. Nguyen, G. Almeida, A macroscopic Washburn approach of liquid imbibition in wood derived from X-ray tomography observations, Sci. Rep. 12 (1) (2022) 1750.
[35] P. Trtik, J. Dual, D. Keunecke, D. Mannes, P. Niemz, P. Stähli, A. Kaestner, A. Groso, M. Stampanoni, 3d imaging of microstructure of spruce wood, J. Struct. Biol. 159 (1) (2007) 46–55.
[36] F. Forsberg, R. Mooser, M. Arnold, E. Hack, P. Wyss, 3D micro-scale deformations of wood in bending: synchrotron radiation μCT data analyzed with digital volume correlation, J. Struct. Biol. 164 (3) (2008) 255–262.
[37] S.J. Sanabria, F. Baensch, M. Zauner, P. Niemz, In-situ quantification of microscopic contributions of individual cells to macroscopic wood deformation with synchrotron computed tomography, Sci. Rep. 10 (1) (2020) 1–16.
[38] A.R. Díaz, E.I.S. Flores, S.J. Yanez, D.A. Vasco, J.C. Pina, C.F. Guzmán, Multiscale modeling of the thermal conductivity of wood and its application to cross-laminated timber, Int. J. Therm. Sci. 144 (2019) 79–92.
[39] J.F. Hunt, H. Gu, P.K. Lebow, Theoretical thermal conductivity equation for uniform density wood cells, Wood Fiber Sci. 40 (2008) 167–180.
[40] M. Louërat, M. Ayouz, P. Perré, Heat and moisture diffusion in spruce and wood panels computed from 3-D morphologies using the Lattice Boltzmann method, Int. J. Therm. Sci. 130 (2018) 471–483.
[41] E.H. Quenjel, P. Perré, Computation of the effective thermal conductivity from 3D real morphologies of wood, Heat Mass Transf. 58 (2022) 2195–2206.
[42] E.-H. Quenjel, P. Perré, Efficient Prediction of the Thermal Conductivity of Wood from Its Microscopic Morphology, Lecture Notes in Mechanical Engineering, 2022, in press.
[43] O. Vay, M. Obersriebnig, U. Müller, J. Konnerth, W. Gindl-Altmutter, Studying thermal conductivity of wood at cell wall level by scanning thermal microscopy (SThM), Holzforschung 67 (2) (2013) 155–159.
[44] J. Eitelberger, K. Hofstetter, Prediction of transport properties of wood below the fiber saturation point–a multiscale homogenization approach and its experimental validation: Part i: Thermal conductivity, Compos. Sci. Technol. 71 (2) (2011) 134–144.

[45] P. Perré, R. Keller, La prédiction des propriétés macroscopiques du matériau bois par sa structure anatomique: besoin ou moyen de caractésiser la paroi?, J. Trace Microprobe Tech. 12 (4) (1994) 277–287.
[46] H. Wang, F. Hou, C. Chang, Experimental and computational modeling of thermal conductivity of cementitious syntactic foams filled with hollow glass microspheres, Constr. Build. Mater. 265 (2020) 120739.
[47] B. Liu, H. Wang, Q.-H. Qin, Modelling and characterization of effective thermal conductivity of single hollow glass microsphere and its powder, Materials 11 (1) (2018) 133.
[48] E.-H. Quenjel, P. Perré, I. Turner, A 3D face interpolated discretisation method for simulating highly anisotropic diffusive processes on general hexahedral meshes, Appl. Numer. Math. 192 (2023) 280–296.
[49] Y. He, Rapid thermal conductivity measurement with a hot disk sensor: Part 1. Theoretical considerations, Thermochim. Acta 436 (1–2) (2005) 122–129.
[50] J.F. Siau, Transport Processes in Wood, Springer-Verlag, New York, 1984.
[51] O. Vay, K. De Borst, C. Hansmann, A. Teischinger, U. Müller, Thermal conductivity of wood at angles to the principal anatomical directions, Wood Sci. Technol. 49 (2015) 577–589.
[52] K. Maeda, Y. Tsunetsugu, K. Miyamoto, T. Shibusawa, Thermal properties of wood measured by the hot-disk method: comparison with thermal properties measured by the steady-state method, J. Wood Sci. 67 (1) (2021) 1–14.
[53] H.P. Steinhagen, Thermal Conductive Properties of Wood, Green or Dry, from -40 to +100 C: a Literature Review, 1977.